PAPER • OPEN ACCESS

Feasibility of raised inner strike point equilibria scenario in ITER for detritiation from beryllium co-deposits

OPEN ACCESS
IOP Publishing | International Atomic Energy Agency
Nuclear Fusion
Nucl. Fusion **63** (2023) 076027 (17pp)
https://doi.org/10.1088/1741-4326/acd9d9

Feasibility of raised inner strike point equilibria scenario in ITER for detritiation from beryllium co-deposits

Jae-Sun Park[1,2,3,*], Xavier Bonnin[2], Richard Pitts[2], Y. Gribov[2], Tom Wauters[2], A.A. Kavin[4], V.E. Lukash[5] and R.R. Khayrutdinov[5]

[1] Oak Ridge National Laboratory, Oak Ridge, TN 37831, United States of America
[2] ITER Organization, Route de Vinon-sur-Verdon, CS 90 046, 13067 St. Paul Lez Durance Cedex, France
[3] Korea Advanced Institute of Science and Technology (KAIST), Daejeon 34141, Korea, Republic Of
[4] Joint Stock Company 'NIIEFA', Doroga na Metallostroy 3, 196641 St. Petersburg, Russian Federation
[5] NRC Kurchatov Institute, Kurchatov sq. 1, 123182 Moscow, Russian Federation

E-mail: parkj@ornl.gov

Received 21 February 2023, revised 9 May 2023
Accepted for publication 30 May 2023
Published 9 June 2023

Abstract

In ITER, tritium retention primarily occurs through co-deposition with beryllium. To avoid exceeding the strict tritium inventory limit, efficient tritium recovery techniques are essential. Baking is the ITER baseline for tritium recovery, but its effectiveness in removing tritium from thick beryllium layers is limited. A raised strike point scenario is considered an alternative method for removing tritium from the ITER inner vertical divertor target by heating components via plasma flux. This paper presents SOLPS-ITER code simulations conducted under various conditions, assessing the divertor performance and tritium outgassing of the raised strike point scenario. As the strike point is raised, recycled neutrals are not efficiently baffled by the dome and scrape-off layer, significantly changing the neutral trajectory and ionization source distribution. This improves detachment accessibility but worsens core-edge compatibility compared to the baseline scenario. However, in the partially detached condition, the impact of raising the strike point, perpendicular transport, and q_{95} on target heat flux is not significant, as it primarily scales with the input power. Target heat flux is translated to target surface temperature using a simplified heat transfer model that considers the 3D target monoblock geometry and active cooling condition, excluding Be layer thermal properties. For partially detached divertor conditions, the bulk tungsten monoblock surface temperature remains below the baking temperature, which is insufficient for efficient tritium outgassing under the actively cooled ITER divertor condition. However, considering the potential thermal contact resistance between the beryllium and tungsten layers, which may significantly impact temperature distribution, the temperature of the beryllium layer can be raised to a level sufficient for efficient tritium outgassing. Therefore, the raised strike point scenario can be considered as an alternative in-vessel tritium removal technique.

* Author to whom any correspondence should be addressed.

Keywords: ITER, raised strike point, detritiation, Be co-deposits, SOLPS-ITER, tritium removal

(Some figures may appear in colour only in the online journal)

1. Introduction[6]

ITER is classified as a nuclear facility and follows nuclear safety regulations. A key safety limit, possibly preventing the completion of the ITER research plan (IRP [1]) is the in-vessel tritium inventory, which has to be kept below 700 g [2]. In view of this limit, tritium recovery techniques are being developed [3]. The in-vessel tritium retention of ITER is predicted to be dominated by co-deposition with beryllium (Be) [4]. A significant fraction of the beryllium, originating from main chamber wall erosion, will migrate to the inner vertical target of the divertor [5–7], where it will cumulate with tritium as co-deposition layers.

ITER foresees divertor baking at 350 °C to recover the tritium from deposits. The effectiveness of this technique, however, is strongly reduced when the layers grow above 50 μm [2], which is likely to occur within one operations campaign. To out-gas tritium from thick layers, much higher temperatures are needed. The IRP [1] proposes to achieve the required temperatures in tokamak pulses in which the inner strike point is raised onto the baffle area. Indeed, the heat flux and corresponding surface temperature increase near the strike point will promote local outgassing. The possibility of running ITER plasmas with raised strike-points was examined in [8]. The study found that for strike points raised to just below the transition region from the straight to curved parts of the vertical W divertor targets, L-mode plasmas up to 14 MA would be controllable in terms of vertical stability. An advantage of the raised strike point scenario is that there is no need to change the active cooling conditions of the divertor, which is time consuming, and the possibility to apply the scenario in dedicated pulses or as part of a tokamak pulse.

A dedicated scenario has been developed using the DINA code [9] that brings the inner strike point to the highest possible point on the divertor baffle. For a given plasma current, the height of the raise is limited by the separation forces in the central solenoid (CS). In this study the plasma current is set at 10 MA which allows reaching about midway the divertor baffle. The L-mode plasma is deuterium-fueled and heated with 20 MW of Electron Cyclotron heating power.

In the scenario considered, the raise of strike points is performed during the plasma current flat-top starting at 42 s (figure 1, start of flat-top (SOF)), using the strategy—the fastest (from the plasma magnetic control point of view) raise of the strike points (mostly inner) followed by the longest (from the plasma magnetic control point of view) return of the strike points to the nominal position just before the end of plasma current flattop (EOF) of 409 s. In the simulation, the EOF correspond to the state when current in CS 1 modules hit the engineering limit (45 kA).

The start of the raising of the (mostly inner) strike point only begins after 200 s (figure 1, start of raising strike point (SOR)), to avoid excessive vertical repulsive forces acting between the CS coils after raise of the strike points. It takes 20 s to reach the highest strike point location (figure 1, end of raising strike point (EOR)). Raising of the strike points (SOR to EOR) faster than during 20 s hits the engineering limit on the voltage in poloidal field coil 6 converter leading to deterioration of the control of plasma-wall gaps. Afterwards, the strike points gradually descend over 160 s and return back to their starting position (figure 1, end of dropping strike point (EOD)). Instead of sweeping the strike point, it is possible to hold it longer at the topmost location, but in that case the duration of the plasma current flattop will be different.

In this paper, the SOLPS-ITER code package [10, 11] is utilized to provide consistent divertor plasma solutions for the DINA scenario, which is needed to properly assess the capability of the raised strike point scenario in promoting tritium outgassing from Be deposited layers. The divertor performance of PFPO-1 phase plasmas and raised strike point scenario plasmas are compared. The surface temperature of the bulk tungsten monoblocks near the strike point, which is the key parameter determining the tritium outgassing rate, is calculated considering the power flux from the plasmas, divertor active cooling, and the 3D divertor monoblock structure. Finally, heat transfer calculations are performed assuming a thermal contact resistivity between Be deposits and the underlying W monoblock as previously done to reproduce the observed temperatures of divertor deposits in JET [12]. It should be noted that the variability of the contact resistance under ITER conditions is not well known, and this study builds upon the understanding from JET experiments. Nevertheless, our findings suggest that the raised strike point scenario could be a promising tritium removal technique in the case of resistive surface deposits.

2. Setup of SOLPS-ITER simulations

The list of SOLPS-ITER (version 3.0.7) simulations utilized in this paper are shown in table 1. The simulations are divided into 8 groups with their representative case name according to the magnetic equilibrium (baseline or raised), grid resolution (standard or refined near scrape-off layer (SOL)), main species (hydrogen (H) or deuterium (D)), (I_p, B_T) combinations

[6] This manuscript has been authored in part by UT-Battelle, LLC, under contract DE-AC05-00OR22725 with the US Department of Energy (DOE). The publisher acknowledges the US government license to provide public access under the DOE Public Access Plan (http://energy.gov/downloads/doe-public-access-plan).

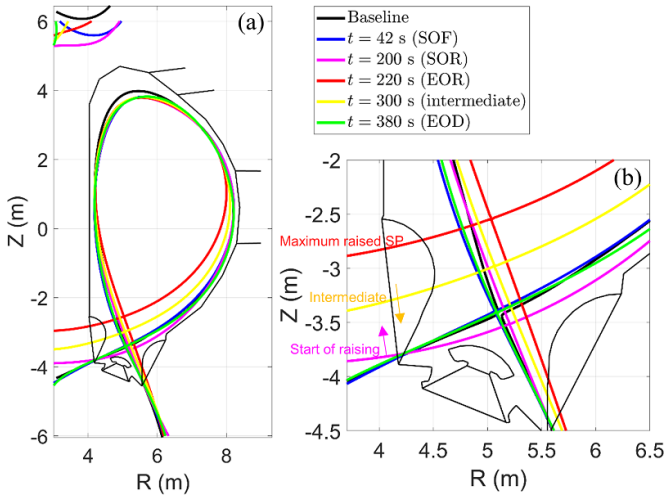

Figure 1. Separatrix lines of the baseline fusion power operation scenario (black) and the raised strike point scenario (colored) are shown for (*a*) the whole region and (*b*) zoomed into the divertor region. Discharge time and the phase of the raised strike point scenario are shown in the legend.

((5 (15) MA, 1.8 (5.3) T) or (10 MA, 5.3 T)), perpendicular transport coefficients $D_\perp$, $\chi_{\perp,i,e}$ (standard or half) and power into the SOL P_{SOL} (20, 40, or 60 MW). These simulations are available from the public ITER IMAS database [13].

The simulation grids of the HST, HST½ and HSOF case series are built based on the ITER baseline scenario equilibrium in fusion power operation phase ('Baseline' in table 1) [1] with I_p = 15 MA and B_T = 5.3 T, giving q_{95} = 3. From the code's perspective, this is equivalent to the representative PFPO-1 phase (I_p, B_T) combinations of 7.5 MA/2.65 T or 5 MA/1.8 T when drifts are not included. Since the location and shape of the separatrix at SOF in the raised strike point scenario is not significantly different from the baseline (figure 1), the same equilibrium and grid have been utilized by multiplying the poloidal flux ψ of the HST grid by ⅔ (see figure 1 in [14]), which essentially only changes the connection length along field lines in SOLPS-ITER. The grid for the HST½ case series is taken from [15], which has the same equilibrium and topology as the HST grid, but for which the mesh has been refined in the near SOL, to be able to properly resolve the steeper profiles just outside the separatrix that are implied by halving the perpendicular transport coefficients. However, to keep the total grid size the same, this leads to a lower grid resolution in the far SOL. The simulation grids of the HRSP, HRSP½, DRSP, DRSP½, and DRSP40MW case series are built based on the ITER raised strike point scenario equilibrium at the 'intermediate' point shown in figure 1. The raised strike point grid with standard grid resolution is shown in figures 2(*a*) and (*b*). For the case series HRSP½ and DRSP½, the grid resolution is adjusted in a similar way to [15].

The HST case corresponds to the SOLPS-ITER database of baseline PFPO-1 scenario plasmas (tungsten divertor surface and divertor fueling conditions) and the detailed simulation setup is available in [14]. For the other cases, the simulation setup is the same as for HST, except for those explicitly mentioned in table 1. For all 8 case series in table 1, a scan on the fuel (H_2 or D_2) gas throughput value has been performed. The divertor neutral pressure p_div ranges from 1 to 11.5 Pa and the divertor condition goes from being attached to partially detached. The anomalous radial ion transport and heat diffusivity coefficients were given as flat profiles with the values in table 1. In all other cases except DRSP40MW and DRSP60MW, P_{SOL} = 20 MW. The cases with P_{SOL} = 20 MW and I_p = 5 MA (HST) or 10 MA (HSOF, HRSP, DRSP) will be staying in L-mode (see figure B-1 in [1]). The case DRSP60MW (I_p = 10 MA) will be operating in H-mode. However, the case DRSP40MW (I_p = 10 MA) will be in a marginal condition of transition between L- and H-mode. Since the power decay length λ_q in H-mode is about half of that in L-mode [16], the transport coefficient of the DRSP40MW and DRSP60MW case series should in principle be adjusted accordingly. However, according to recent XGC1 simulation results [17], λ_q is expected to move away from the $1/I_\mathrm{p}$ experimental scaling [18] to a turbulence-driven scaling at $I_\mathrm{p} \sim$ 8 MA. Since the raised strike point scenario has I_p = 10 MA, where the effect of this change of physics regime should start to be noticeable, the uncertainty on the value of λ_q remains quite large. Therefore, in this paper, rather than following a specific scaling, the perpendicular transport coefficients used in the SOLPS-4.3 burning plasma database (see [19] and table 1 in [14]) were collectively applied, and a factor of 2 lower values were used only for the ½ transport cases. As shown later, operation of the raised strike point scenario is only acceptable in detached conditions, for which the change of λ_q by factor of 2 does not have a significant effect on the peak heat flux. Sputtering from plasma-facing components is not considered here. Helium ash is also not relevant for these cases because of the low P_{SOL}. The divertor target material is set as tungsten, assuming no deposited beryllium on the surface. The fuel gas puff location is set as a surface in divertor region below the dome (figure 2(*b*)). Note that in the partially detached regime of PFPO-1 plasmas (without impurity seeding and with P_{SOL} = 20 MW), the selection of the target surface material and the gas puff location do not make a significant difference in divertor plasma performance [14].

3. Overall divertor plasma performance of the raised strike point scenario

This section is for a general discussion of the divertor solution before using the heat loads to the surfaces in the next section. The neutral trajectory that was changed by raising the strike point and its effect on divertor performance were analyzed. In particular, the focus was on the change in detachment behavior. Based on this, a feasible operation regime was suggested.

Table 1. List of the SOLPS-ITER simulation discharges utilized in the main content of this paper, as available from the public ITER IMAS database. IMAS shot numbers are composed of 6 digits, with a two-digit main fuel species prefix (10: hydrogen, 11: helium, 12: deuterium), followed by a unique four-digit number.

Case name	Species (IMAS prefix)	Magnetic equilibrium	Grid resolution	Remarks	I_p (MA)	B_T (T)	$D_\perp$ ($m^2 s^{-1}$)	$\chi_{\perp,i.e.}$ ($m^2 s^{-1}$)	IMAS shot numbers
HST	H (10-)	Baseline	Standard	PFPO-1	5 (15)	1.8 (5.3)	0.3	1.0	3054–3062
HST½	H (10-)	Baseline	Refined near SOL	½ ⊥ transport	5 (15)	1.8 (5.3)	0.15	0.5	3112–3114
HSOF	H (10-)	Baseline ($\frac{2}{3}\psi_{standard}$)	Standard	SOF	10	5.3	0.3	1.0	3083–3091
HRSP	H (10-)	Raised SP	Standard	—	10	5.3	0.3	1.0	3092–3101
HRSP½	H (10-)	Raised SP	Refined near SOL	½⊥ transport	10	5.3	0.15	0.5	3115–3117
DRSP	D (12-)	Raised SP	Standard	RSP scenario	10	5.3	0.3	1.0	3102–3111
DRSP½	D (12-)	Raised SP	Refined near SOL	½⊥ transport	10	5.3	0.15	0.5	3118–3120
DRSP 40 MW	D (12-)	Raised SP	Standard	P_{SOL} 40 MW	10	5.3	0.3	1.0	3121–3124
DRSP 60 MW	D (12-)	Raised SP	Standard	P_{SOL} 60 MW	10	5.3	0.3	1.0	3131–3134

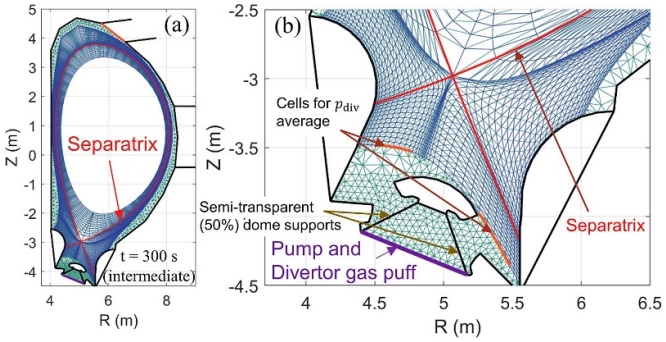

Figure 2. SOLPS-ITER simulation grids of the (*a*) raised strike point equilibrium at the intermediate phase (HRSP, DRSP, DRSP40MW, DRSP60MW). (*b*) Zoomed into divertor region. The grid for the ½ perpendicular transport cases (HST½, HRSP½, and DRSP½) has a different resolution distribution being more refined in the near SOL but coarser in the far SOL but with the same total grid size (not shown).

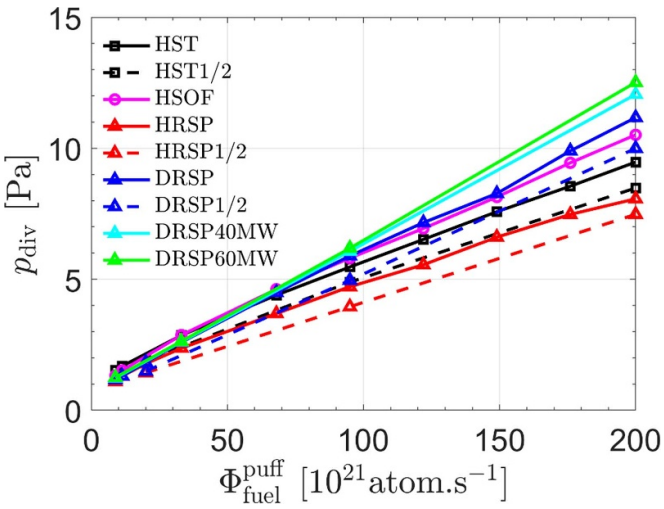

Figure 3. Divertor neutral pressure as a function of fuel throughput $\Phi_{fueling}$.

3.1. Neutral dynamics

The plasma and neutral parameters in this paper are mainly parameterized by p_{div}. To be consistent with previous studies, the p_{div} average neutral pressure for the HST case series is computed from the same locations as in the SOLPS-4.3 burning plasma and SOLPS-ITER PFPO-1 plasma databases [14, 19]. Those locations correspond to the edge cells of the field-aligned grid directly facing either entrance to the sub-divertor volume in which the pumping duct is located (see figure 1 in [14]). For the raised strike point equilibrium, the same location criterion is used (figure 2). A similar trend to the HST is found, i.e. p_{div} is linearly proportional to the fuel throughput and the linearity is maintained from attached to detached divertor conditions (figure 3). Note that the DRSP cases has 20%–40% higher p_{div} than the HRSP cases for a given fuel throughput.

To achieve global particle balance, the gas puffing (as molecules) and the pumped out particles (more than 99% are molecules), which are the dominant net particle source and sink, should be equalized. The pumped out fluxes are calculated as the product of the pumping speed and the neutral pressure in front of the pumping surface. The pumping speed is proportional to the local thermal velocity. Since molecules near the pump are thermalized with the wall temperature through multiple reflection(s), the local thermal velocity of the H_2 molecules is higher than that of the D_2 molecules by a factor of the square root of the mass ratio. Therefore, the neutral pressure in front of the pump should be higher by the same factor for DRSP cases than for HRSP cases to achieve the same pumped flux. Indeed, the SOLPS-ITER results demonstrate that the pressure in front of the pump is linearly proportional to the fuel throughput, and D plasmas have a pressure

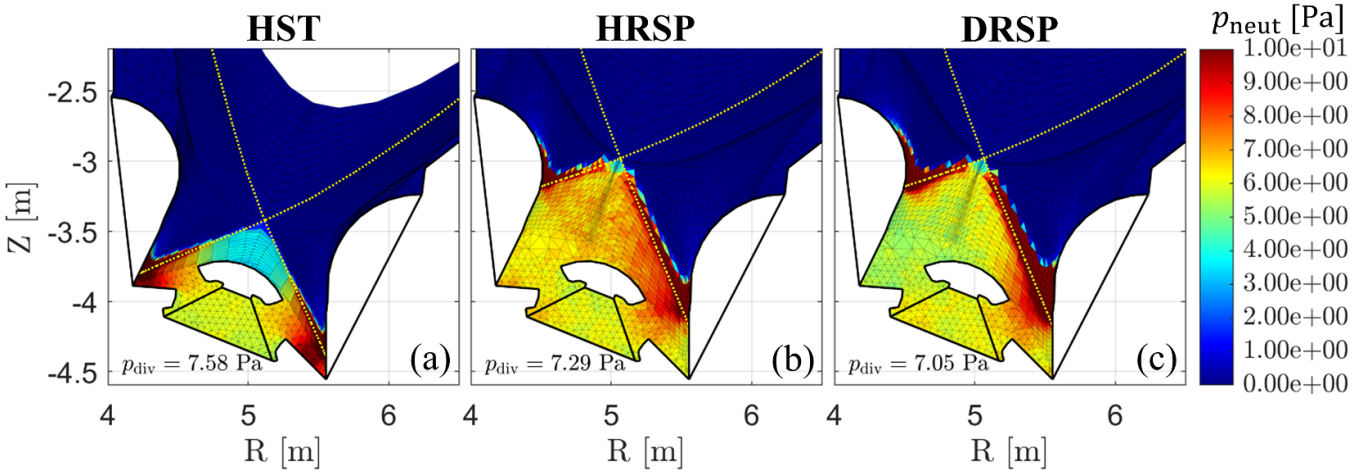

Figure 4. Two dimensional neutral pressure distribution of the cases HST, HRSP, DRSP for p_{div} = 7–8 Pa, which correspond to the partially detached condition. Both atom and molecule contributions to the neutral pressure are considered.

1.30–1.43 times greater than H plasmas, regardless of magnetic configuration. The neutral pressure in front of the pump is proportional to p_{div} [14], so the species dependence of p_{div} comes from the difference in pumping speed resulting from the difference in mass. The slight difference in p_{div} between the standard resolution grid and the refined near SOL grid is due to the shift in location of the p_{div} averaging surface as the grid resolution redistributes. In the JET experiment [20], for the same reason as above, the divertor neutral pressure of D plasmas is higher than that of H plasmas.

The two-dimensional distribution of neutral pressure for the partially detached regimes (p_{div} =7–8 Pa) of HST, HRSP, and DRSP cases are shown in figure 4. Both the atom and molecule contributions to the neutral pressure are included. There are significant differences in the pressure distribution below the X-point, above the dome. In the HST case, the dome effectively screens neutral particles, whereas in the HRSP and DRSP cases, there is no significant difference in neutral pressure between above and below the dome. Most of the recycled neutral particles from the target ionize when they reach the SOL region, which is much more opaque than the private flux region (PFR). Each time neutral particles are reflected off the wall, the proportion of molecules increases (the reflection model assumes that molecules remain molecules, while atoms recombine together with a certain probability). In the HST case, most of the thermalized molecules reflected from the wall enter the SOL directly or reflect back from the dome, so the probability of reaching the area between the dome and the X-point is small. On the other hand, for the HRSP and DRSP cases, the PFR region extends much further above the dome, so all the PFR region is easily accessible to the reflected neutrals, including the area below the X-point. Therefore, except for near the strike point and near the SOL–PFR interface where ionization/dissociation occurs actively, a relatively uniform distribution of neutral pressure is established.

This can also be illustrated by viewing sample recycling neutral trajectories computed by EIRENE, the neutral kinetic transport module within SOLPS-ITER (figure 5). Recycled

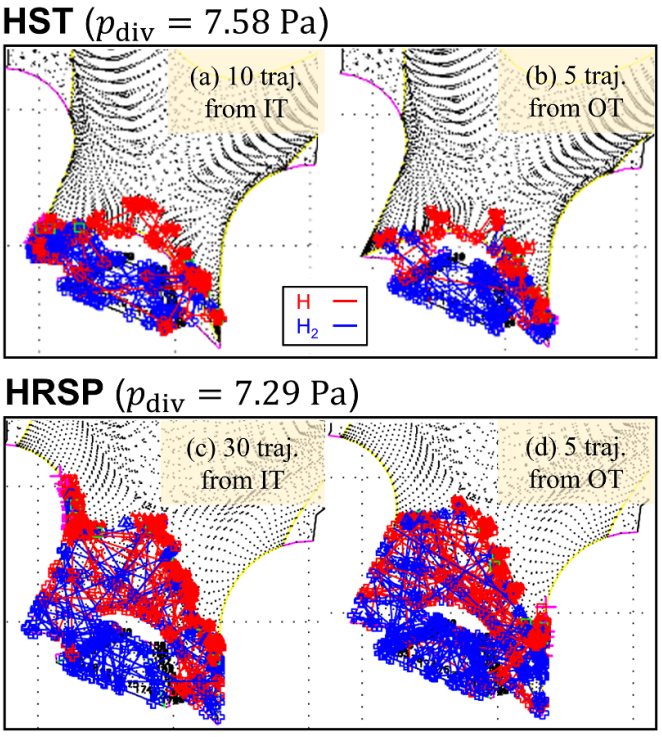

Figure 5. EIRENE sample trajectories of particles launched from both targets. The cases of HST and HRSP are shown for p_{div} =7–8 Pa. (*a*) HST, 10 trajectories launched from inner target (*b*) HST, 5 trajectories launched from outer target (*c*) HRSP, 30 trajectories launched from inner target (*d*) HRSP, 5 trajectories launched from outer target.

neutrals are mostly launched from the near SOL target region, according to the incident ion flux profile. In the HST case, most of the trajectories sampled in the near SOL region along both targets are directed towards the PFR, and are ionized quickly, before they manage to cross the separatrix. A few enter the PFR and bounce back off the reflector plates (the quasi-horizontal plates that form the 'corner' with the vertical

targets), and then ionize near the strike point (figures 5(*a*) and (*b*)). Some of the neutrals can travel to the other side of the target through the space below the dome. Trajectories originating from either target display nearly symmetric distributions. The thermalized molecules that travel to the area between the X-point and the upper side of the dome is limited because the gap between the dome and the SOL, which is the most probable channel leading to this zone, is narrower compared to the raised strike point cases and that most of them are screened by the SOL and dome.

With the raised strike point equilibrium, there is a big difference in recycled particle trajectories between those launched from the IT versus the OT. As in the HST case, since the outer strike point is still close to the corner, the outer reflection plate can reflect some portion of the recycled particles, causing them to immediately ionize near the outer strike point. Trajectories that do not intersect the outer reflection plate enter the space below the dome, and are reflected many times with high probability before exiting the gap. Therefore, these trajectories are long and lead to a more diffuse neutral density rather than concentrated near the target (figure 5(*d*)). However, since the gap between the dome and the outer SOL is wider than in the HST case, trajectories that exit through the gap are evenly distributed along the inner SOL-PFR boundary and even reach near the X-point. The inner strike point is far from the inner reflector plate, thus it is hardly affected by the corner, and recycled neutrals that enter the PFR pass through there with relatively low neutral opacity (ballistically), and most of them reach the outer SOL-PFR boundary, or reflect from the upper side of the dome and reach the outer SOL-PFR boundary relatively uniformly, before they ionize. A distinctive feature of trajectories that are launched from the inner target (IT) of the HRSP case is that, in the SOL region, there are noticeably more trajectories that are immediately ionized along the target. Along the inner vertical target, the curvature changes rapidly from the strike point to the far SOL (figure 2(*b*)), so the main direction of the recycled neutrals gradually changes from the PFR to the SOL. Therefore, the proportion of recycled neutrals that are immediately ionized in the SOL, which has a much higher neutral opacity than the PFR, increases. More sampling is required to observe the neutral dynamics passing through the PFR, so 6 times more trajectory than from the outer target case are shown to improve visibility. These observations are consistent with the results of DIVGAS simulations in the European DEMO ITER-like divertor configuration, showing that the dome improves neutral compression and shows strong reflux of molecules to the X-point vicinity in the absence of the dome [21]. With the raised strike point, the influence of the dome on neutral screening is relatively small, which increases the likelihood of onset of thermal instability near the X-point (MARFE).

3.2. Detachment behavior

Two-dimensional distributions of electron density, electron temperature, and radiated power for the partially detached regime (p_{div} =7–8 Pa) in the HST, HRSP, and DRSP cases are shown in figure 6. As explained in section 3.1, the recycled neutrals in the HRSP and DRSP configurations can access the full length of the SOL-PFR boundary, so the density peaks there, while the electron density only peaks near the targets in the HST case (figures 6(*a*)–(*c*)). Note that the flow velocity pattern does not show significant differences between the standard and raised strike point configurations. Likewise, electron cooling is most intense at the location of the electron density peak (figures 6(*d*)–(*f*)). Regarding the lobe-like region, where the flow velocity reverses in the OT (indicated by the magenta color), this expands as the p_{div} increases (as the divertor condition transitions from attached to detached). This expansion is observed not only in the HST case but also in the RSP cases. However, it appears more clearly in the HST case due to a higher detachment threshold and a much slower rollover drop in target flux compared to the RSP cases, which results in larger recycled neutrals and ionization sources (refer to figure 8(*b*)).

As usual, the 5 eV front, or so-called 'ionization front', moves upstream away from the target as the divertor neutral pressure increases and the condition changes from attached to detached. For the HRSP and DRSP cases, the ionization front also moves radially from the strike-point region towards the far SOL. Therefore, the near SOL is very efficiently cooled, over a wider radial extent in the RSP configuration. This can be partly attributed to the larger amount of neutrals coming from the OT to the IT in the RSP cases. In the HST case, most of the recycled neutrals are ionized immediately near the targets, and cooling proceeds by pushing the ionization front upward, a process mostly limited to the near SOL. Dense and cooler regions with higher neutral density have a higher radiation emissivity (figures 6(*g*)–(*i*)). Indeed, the HRSP and DRSP cases show significant X-point radiation, and this may be one of the limitations of operating raised strike point equilibria, although there is an advantage that the neutral behavior results in a lower detachment threshold.

By comparing HRSP and DRSP cases, the isotope effect on the divertor condition can be characterized. In the SOLPS-ITER simulations used in this paper, the only isotope effect is the difference in mass between H and D. Properties such as particle and energy reflection coefficients from the TRIM [22] database (from SOLPS-ITER version 3.0.7) do not show significant differences between H and D when incident on a tungsten surface (<5% for the incident ion energy range of 1–10^4 eV). In HRSP and DRSP cases, the neutral density (and neutral pressure) peaks along the SOL-PFR boundary (figures 4(*b*) and (*c*)) where the electron temperature is a few eV and recycled neutrals have a larger mean free path than in other parts of the SOL. The D neutrals are slower than the H neutrals due to the mass differences and this is supported by fast temperature equilibration between electrons and ions in the SOL near the target. Therefore, D neutrals travel for a longer time, yielding a larger density in a wider region. This enhances plasma–neutral interactions and improves accessibility to detachment. Consequently, D plasmas have a better near SOL plasma cooling efficiency (figures 6(*d*)–(*f*)) and a wider radiation zone (figures 6(*g*)–(*i*)) than H plasmas.

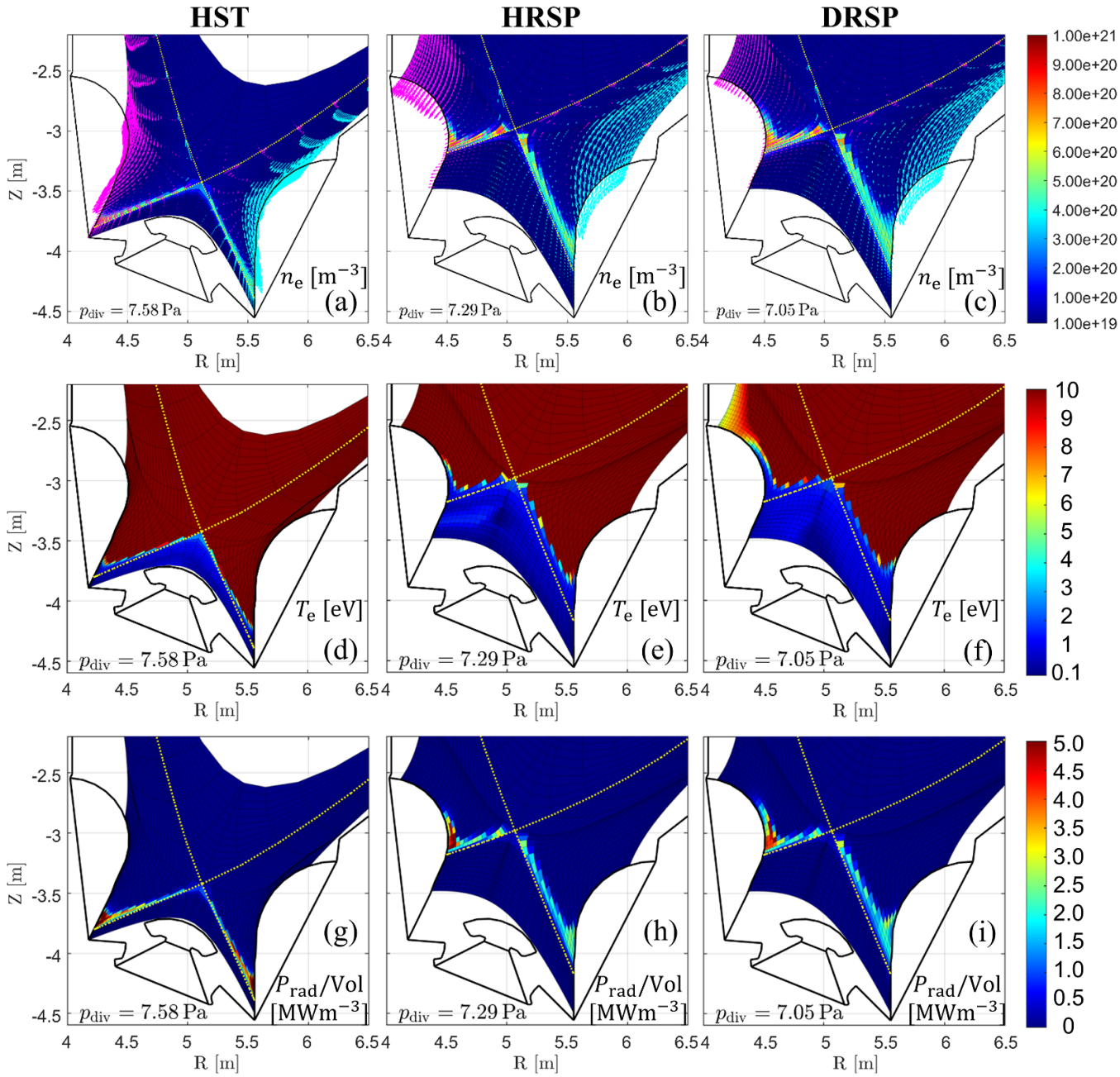

Figure 6. Two-dimensional distribution of (*a*)–(*c*) electron density and ion flow velocity (*d*)–(*f*) electron temperature (*g*)–(*i*) radiated power per volume. The HST, HRSP, and DRSP cases for p_{div} = 7–8 Pa are shown columnwise from left to right, respectively. Flow velocity is represented by arrows, with cyan indicating flows from the IT to the OT in the poloidal direction, and magenta representing flows from the OT to the IT. The length of the arrows is proportional to the velocity magnitude.

The total radiated fractions of the HST, HRSP, and DRSP cases are 10%–40%, 10%–50%, 20%–75% of P_{SOL}, respectively (figure 7). The cases with ½ transport coefficients exhibit a lower radiated power fraction. As explained above, the radiation zone of the DRSP is wider than that of HRSP, and the total radiation is 20%–35% higher for given p_{div}, due to the isotope (mass) effect. One measure of neutral leakage from the divertor to upstream can be expressed as $(S_{iz}^{core} + S_{iz}^{SOL})/S_{iz}^{total}$, which is the ratio of the ionization sources above the X-point to the total ionization sources (figure 8(*a*)). Since the neutrals provide ionization sources not only near the strike point, but also near the X-point along the SOL-PFR boundary in HRSP and DRSP cases, there is a factor of 10 higher neutral leakage than in the HST case. However, the total ionization source, which is dominated by the recycled neutrals from both targets, decreases much faster after rollover (figure 8(*b*)). This is because the radiated fraction of the HRSP and DRSP cases is greater than that of the HST, and that less energy can be used for neutral ionization (power starvation) [23]. The increased neutral leakage and reduced total ionization

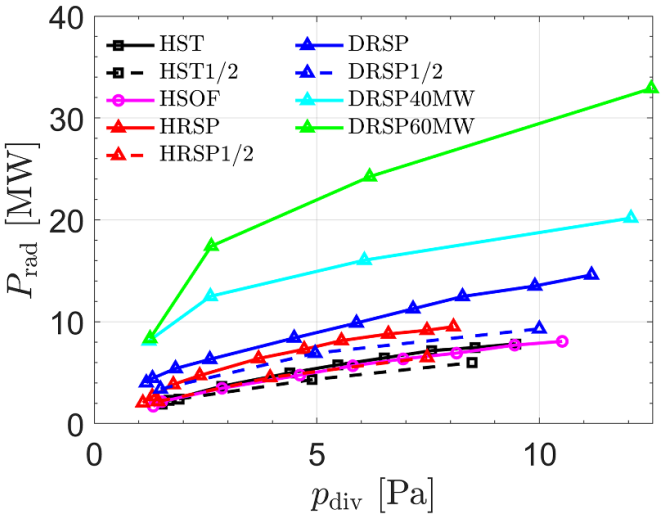

Figure 7. Total radiated power as a function of p_{div}.

compensate so the upstream density saturates for all cases (figure 8(*c*)).

3.3. Role of plasma–neutral interactions on detachment behavior

In this paper, only pure hydrogenic cases are considered, without any extrinsic impurities. Thus, the divertor condition and the plasma–neutral interaction regime are mostly determined by the target electron temperature. Plasma–neutral interactions mostly occur immediately next to the target in attached conditions. In detached conditions, the divertor SOL flux tubes are cooled, creating an environment in which plasma–neutral interactions can occur actively even relatively far upstream, and reactions involving molecules and volumetric RC become significant.

The target electron temperature T_{et} is strongly correlated with the target neutral density and the average neutral density in the flux tube [14, 24]. Figure 9 shows the locations of the 1, 2, and 5 eV fronts in terms of the $s_{\|}$ normalized coordinate for the parallel connection length from the target to the mid-plane, as a function of T_{et}. The location of the X-point along $s_{\|}$ is slightly different for each flux tube and configuration, so the corresponding ranges are indicated in yellow and green shades for the HST and HRSP (DRSP) cases, respectively. These fronts roughly correspond to the locations of the onset of volumetric RC, charge exchange with molecules, and ionization, respectively. The 1 eV front (figure 9(*a*)) is located at a similar $s_{\|}$ between the baseline and the raised strike point cases. However, the 2 and 5 eV front positions (figures 9(*b*) and (*c*)) are more upstream for the HRSP (DRSP) case than for the HST case for a given T_{et}. In other words, the raised strike point case shows more efficient flux tube cooling than the baseline case under conditions of similar average neutral density within the flux tube [14].

The change in the parallel electron temperature distribution also leads to a difference in the location of the reaction centers of mass (CM), defined for reaction R as:

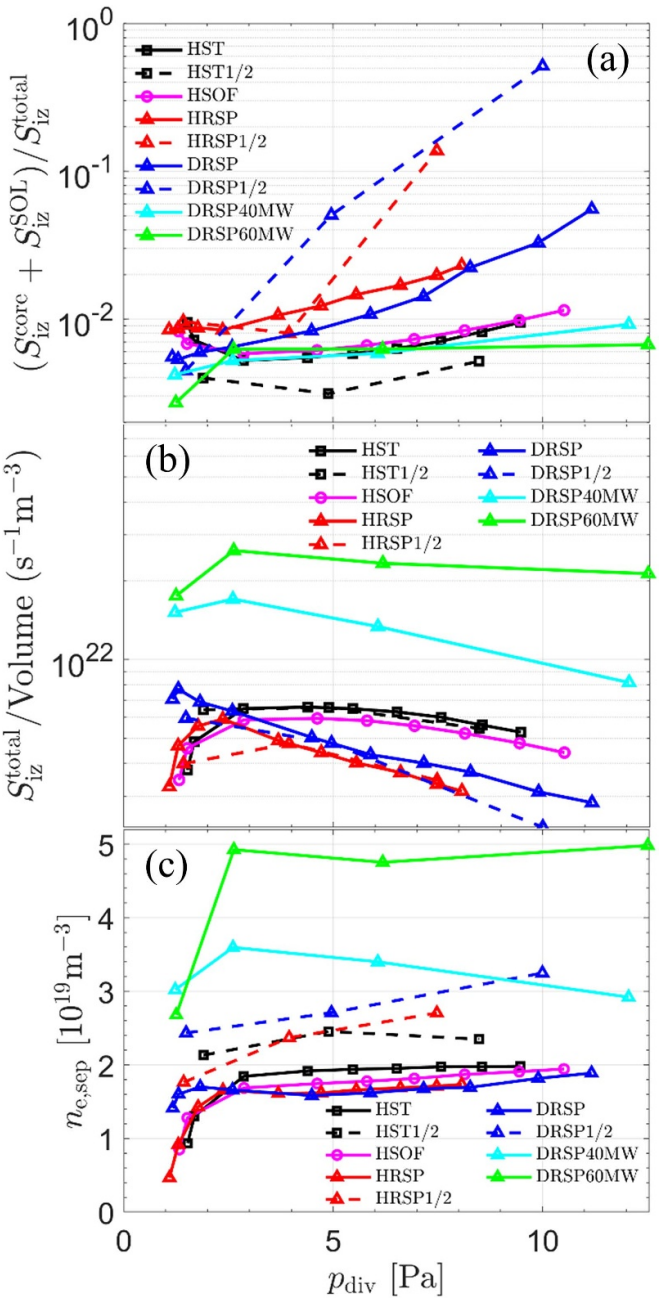

Figure 8. (*a*) Sum of ionization source from core and SOL divided by total ionization source (*b*) total ionization source per volume (*c*) outer midplane separatrix electron density as a function of p_{div}.

$$s_{\|,CM}^{R} \equiv \frac{\int_t^u S_R s_{\|} ds_{\|}}{\int_t^u S_R ds_{\|}} \quad (1)$$

where S_R corresponds to the source rate for reaction R, while u and t correspond to the upstream (mid-plane) and target locations, respectively. The center of reactions for electron impact ionization (EI), molecular charge exchange (mol. CX), and volumetric RC are shown in figure 10. Since the ionization cross-section roughly follows the ionization potential, it is sensitive to the electron temperature. The CM of EI, which can be identified as the 'ionization front', gradually moves upstream as p_{div} increases (and T_{et} decreases) (figure 10(*a*)),

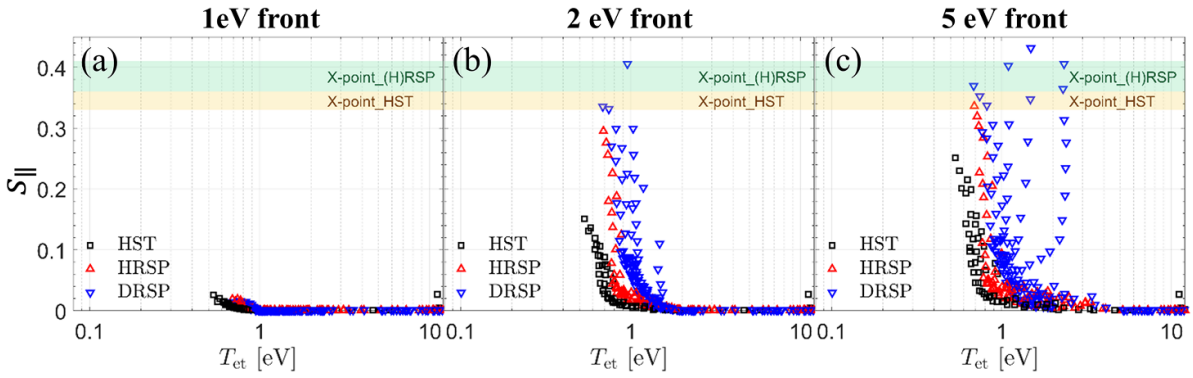

Figure 9. Normalized parallel coordinate for 1, 2, and 5 eV in the SOL flux tube as a function of target electron temperature. The X-point locations (depending on the radial coordinate and magnetic geometry) are indicated by shading. All SOL rings are included for the discharges 103054–103062 (HST), 103 092–103 101 (HRSP), and 123 102–123 111 (DRSP). SOL rings are used to distinguish flux tubes in the SOLPS code, representing a set of cells along the poloidal direction in the SOL region for a specific radial index on the SOLPS grid. The SOL ring index is differentiated by radial cell index.

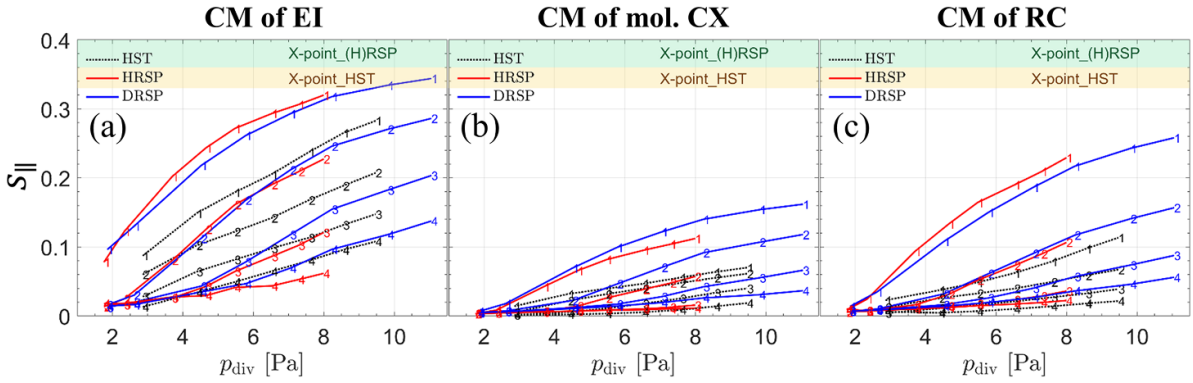

Figure 10. Centers of mass of the plasma–neutral interactions for 1st to 4th SOL rings are represented along the normalized parallel coordinate as a function of p_{div}. (*a*) Main ion source from atom–electron interaction (*b*) momentum source from the molecule–plasma interaction (*c*) main ion sink from volumetric recombination. The X-point location (depending on the radial coordinate and magnetic geometry) are indicated by shading.

following the 5 eV front. The mol. CX rate largely depends on molecular density, so it becomes important only when molecules begin to accumulate as T_{et} is cooled down to a few eV [14, 25]. As the flux tube cools down, the mean free path of molecules towards upstream becomes longer, so as p_{div} increases (and T_{et} cools), the CM of mol. CX moves upstream (figure 10(*b*)). Similarly, cooling of the flux tube means the expansion of the area where RC can occur, so as p_{div} increases (or T_{et} cools), the CM of RC moves upstream. A consistent pattern emerges on which the various CMs are located more upstream for the HRSP (DRSP) cases is than for the HST case (figure 10(*c*)).

One can also apply the extended two-point model formalism [26, 27] to the SOL flux tubes. Critical parameters are the momentum and power loss fractions, defined as the loss ratio of total pressure and internal energy from upstream (taken as the X-point here) to downstream (target), respectively. By breaking down the loss factors into their various contributions, it is possible to figure out which mechanisms mainly contribute to the detachment. These contributions are plotted along the 2nd SOL ring, chosen as representative of the near SOL while being less affected by radial transport (figure 11). In the HST case, the momentum loss is mainly dominated by the atom–plasma reactions at low p_{div}, but the influence of molecules grows with increasing p_{div} [14] (figure 11(*a*)). In the raised strike point cases (figures 11(*b*) and (*c*)), along with this tendency, the effect of volumetric RC becomes significant from about $p_{div} > 3$ Pa. This is consistent with the fact that the CM of RC is located more upstream than for the HST case due to better flux tube cooling (figure 10(*c*)). RC transfers momentum away from the plasma to the neutrals. From the point of view of power loss, atom–electron interactions, that is, ionization and radiation, are the dominant contributors (figures 11(*d*)–(*f*)). The effect of RC on power loss is almost negligible. In HRSP and DRSP cases, most of the power loss is due to radiation. This is because, in the raised strike point cases as described in section 3.2, cooling occurs efficiently along the SOL-PFR boundary in the near SOL as well as near the X-point, so that the radiation zone is distributed much more widely than in the HST case (figures 6(*g*)–(*i*) and 7).

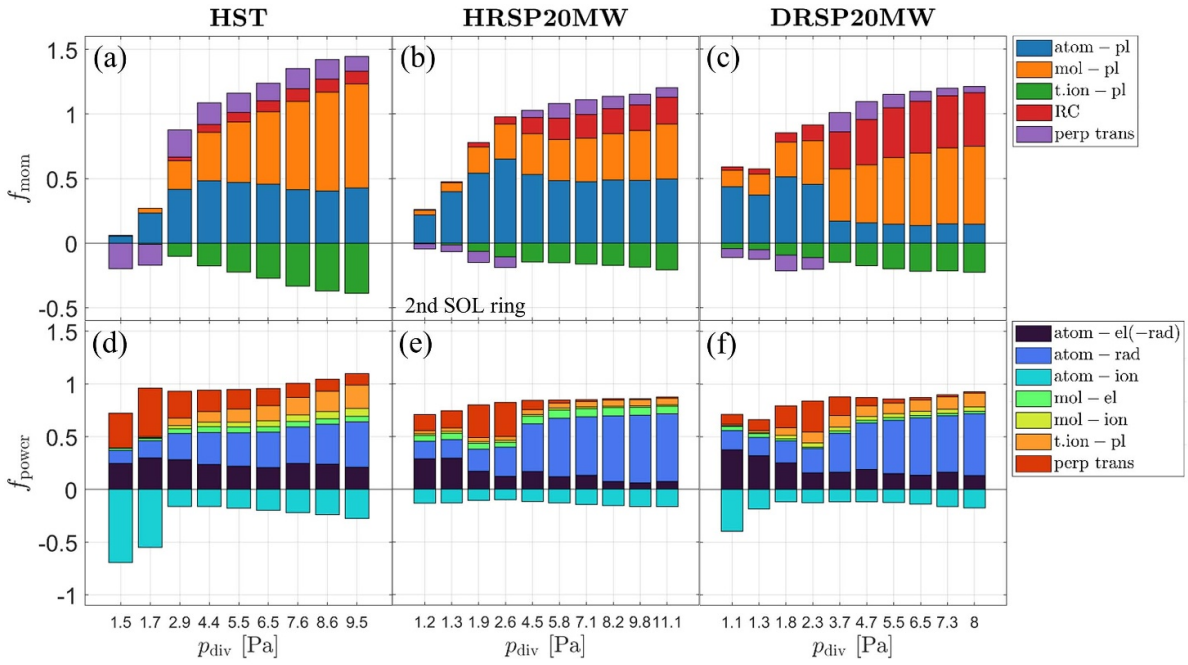

Figure 11. (*a*)–(*c*) Inner SOL momentum loss factor decomposed into most dominant causes along the 2nd SOL ring. In the legend, atom-pl, mol-pl, t.ion-pl, RC, and perp trans corresponds to atom–plasma interactions, molecule–plasma interactions, test ion (H_2^+ or D_2^+)-plasma interactions, volumetric recombinations, and perpendicular transport. (*d*)–(*f*) Inner SOL power loss factor decomposed into most dominant causes along the 2nd SOL ring. In the legend, atom-el-(-rad), atom-rad, atom-ion, mol-el, mol-ion, t.ion-pl, perp trans corresponds to atom–electron interactions except for the atom radiated power, atom radiation, atom–ion interactions, molecule–electron interactions, molecule–ion interactions, test ion–plasma interactions and perpendicular transport. The upstream position is taken as X-point.

3.4. Feasible operation regime

Physical sputtering of tungsten is one of the limiting factors for sustainable ITER diverted plasma operation, and the raised strike point scenario must stay below the tungsten concentration limit [28] to be viable. According to SDTrimSP [29] calculations, the tungsten physical sputtering yield Y_{phys} when D^+ ion incident on changes by 3 orders of magnitude as the electron temperature at the sheath entrance varies over the T_e =30–100 eV [30, 31]

$$Y_{phys} \sim \begin{cases} 10^{-3} & \text{for} \quad T_e = 100\,\text{eV} \\ 10^{-4} & \text{for} \quad T_e = 50\,\text{eV} \\ 10^{-6} & \text{for} \quad T_e = 30\,\text{eV} \end{cases} . \qquad (2)$$

In addition to the Y_{phys} changes in T_e according to the D^+ incidence, another factor that demands the maintenance of a lower T_e level is the prompt redeposition of sputtered tungsten, which is particularly effective in partially detached conditions. The ionization potential of tungsten is about 8 eV, so it is relatively easy to ionize near the target. Since tungsten ions have a relatively large gyro radius, if sputtered tungsten is ionized within a distance of the order of the gyro-radius near the target, it is likely to be immediately re-deposited on the target and will not contribute to effective sputtering. This prompt redeposition process is highly dependent on the ionization location and is therefore sensitive to the main plasma background density and temperature. It is also sensitive to T_i/T_e because its force balance is governed by electric and thermal forces in the sheath [32]. According to the ERO-PIC calculation result in [33], the rate of prompt redeposition f_{prompt} is 0.6–0.9 for sheath entrance plasma parameters most similar to those of ITER: T_e = 5–20 eV, $n_e = 6 \times 10^{19}\,m^{-3}$. In this range of T_e, the W self-sputtering rate will be only 10^{-3} to 10^{-2} ([34]). Therefore, the effective physical sputtering rate is further reduced by one order of magnitude from the above SDTrimSP result.

Assuming no impurities and equilibration between T_e and T_i, equation (2) implies that the plasma temperature in front of the targets must remain below 30 eV for sustainable operation, at least in the flux tubes where the ion flux is significant. However, if even a small percentage of Be impurities is included, the data from [30] show that the sputtering yield at low temperature is fully dominated by the incident Be^{2+} ions, and that the plasma temperature at the target must be further lowered to below 5 eV, i.e. partially detached conditions. Figure 12 demonstrates the maximum T_{et} in the range of $(r - r_{sep})_{OMP} < 0.02$ m at both targets. Clearly, the attached regime of HST(½) and HRSP(½) shows electron temperatures that would yield much too high a tungsten sputtering yield and operation conditions are limited to the region above 7 Pa where T_{et} at both targets drop below 5 eV. Note again however that the raised strike point cases detach at lower p_{div} than the HST cases along the IT. At the same time, the HRSP and HST cases are showing similar cooling rates at the outer target while the DRSP cases detach earlier due to the isotope effect. Therefore, the operation regime of the DRSP(½) case is relaxed compared to the hydrogen cases, and it is expected to be feasible when the p_{div} is 4–5 Pa or more.

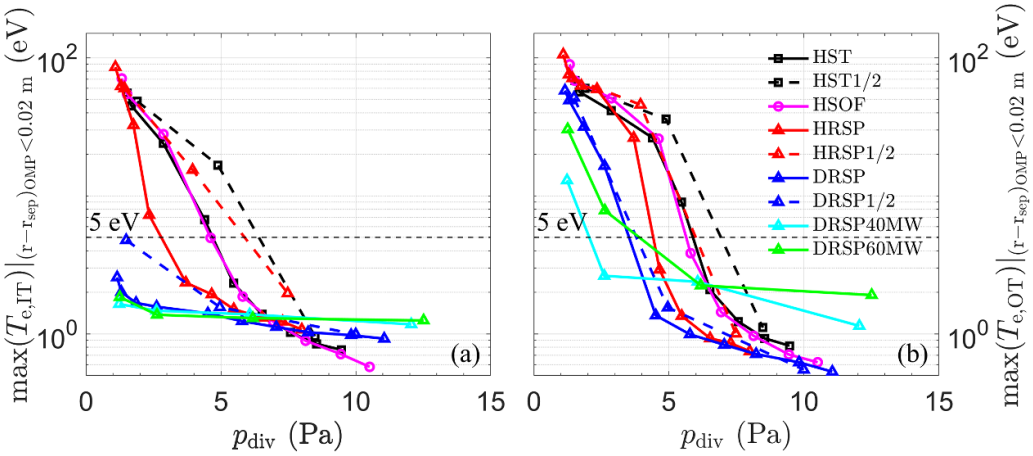

Figure 12. Maximum target electron temperature in the range of distance from the strike point mapped to OMP smaller than 0.02 m for (*a*) inner target and (*b*) outer target. A 5 eV reference is indicated by a dashed line.

4. Target heat load and surface temperature

The aim of the raised strike point scenario is to locally increase the surface temperature along the upper part of the inner divertor target to promote tritium outgassing in that area. In this section, the plasma heat flux reaching the target is calculated from SOLPS-ITER. Then, a FEM analysis is performed using a simplified plasma-facing component model [35] to calculate the target surface temperature. Based on that result, the tritium removal performance of the raised strike point scenario is assessed.

4.1. Target heat flux

To protect leading edges, the ITER divertor cassettes are tilted about 0.5° toroidally and the toroidal shaping on the top surface of the monoblocks is about 1.0°. The perpendicular heat fluxes in SOLPS-ITER $q_{\perp}^{\mathrm{cyl}}$ are considered to be deposited onto toroidally symmetric target surfaces so they need to be multiplied by a correction factor $f_{\mathrm{tilt,shape}}$ to take this tilting and shaping into account [35]. This correction factor can be written as follows:

$$q_{\perp}^{\mathrm{tilt,\ shape}} = q_{\perp}^{\mathrm{cyl}} \times f_{\mathrm{tilt,\ shape}} = \frac{q_{\parallel} A_{\parallel}}{A_{\perp}^{\mathrm{cyl}}} \times f_{\mathrm{tilt,shape}} = \frac{q_{\parallel} A_{\parallel}}{A_{\perp}^{\mathrm{cyl}}} \times \frac{\sin(\theta + 1.5°)}{\sin(\theta)} = q_{\parallel} \times f_{\mathrm{total}} \quad (3)$$

where θ is the angle of incidence of the magnetic field onto the monoblock surface and $A_{\parallel}$, $A_{\perp}$ are the flux tube surface areas parallel to the magnetic field and perpendicular to the monoblock surface (without consideration of tilting and shaping), respectively. The angle of incidence on the IT is shown in figure 13(*a*) as a function of radial coordinate with respect to the separatrix mapped to the inner mid-plane. It is determined by the local magnetic field and the PFC geometry so it is radially varying but largely determined by q_{95}. The ratio $A_{\parallel}/A_{\perp}^{\mathrm{cyl}}$ is proportional to $\sin(\theta)$ as shown in figure 13(*b*). Smaller θ yields larger $f_{\mathrm{tilt,shape}}$ (figure 13(*c*)) since it is a decreasing function of θ in the range of $(0°, 90°]$. Finally, f_{total} can be written as $\sin(\theta + 1.5°))$, which is an increasing function of θ but only approximately linear for small angle.

Considering tilting and shaping, the profiles of the perpendicular IT heat flux $q_{\perp,\mathrm{IT}}$ (omitted 'tilt, shape' on the superscript), which includes contributions from the plasma, neutrals, and radiation, are shown (figure 14). For all cases, as p_{div} increases, the near SOL detaches: the $q_{\perp,\mathrm{IT}}$ peak decreases and it moves radially outwards. The half transport cases have a factor of 1.3–2.5 times higher $q_{\perp,\mathrm{IT}}$ than the standard transport coefficient cases in the attached regime. However, in detached conditions, $q_{\perp,\mathrm{IT}}$ only differs by 10%. Changing q_{95} or the magnetic field configuration does not affect the target heat flux profile significantly. However, when the heating power itself is increased, the peak heat flux is increased by a factor of 2 or 3 (DRSP40MW or DRSP60MW) compared to DRSP even in the detached regime. Figure 15 shows the various contributions from plasma, neutrals, and radiation to $q_{\perp,\mathrm{IT}}$. Compared to the baseline magnetic configuration, the raised strike point cases can be seen to have a significantly increased radiation load, and this is consistent with the total radiated power (figure 7). However, since the radiation front is moving upstream and radially outward as p_{div} increases, the radiation contribution to the peak is not necessarily proportional to the total radiated power. As p_{div} increases, the plasma heat load steadily decreases. The reduction is faster in HRSP and DRSP cases than in the HST case, as near SOL detachment is achieved faster in the raised strike point scenario, as described in section 3.2. However, since this is compensated by the higher radiation heat load, there is no significant difference in the end in the total $q_{\perp,\mathrm{IT}}$. In the half transport cases, once the near SOL plasma is detached, the peak heat flux contributed by the plasma does not show much difference from the standard transport cases. In addition, since

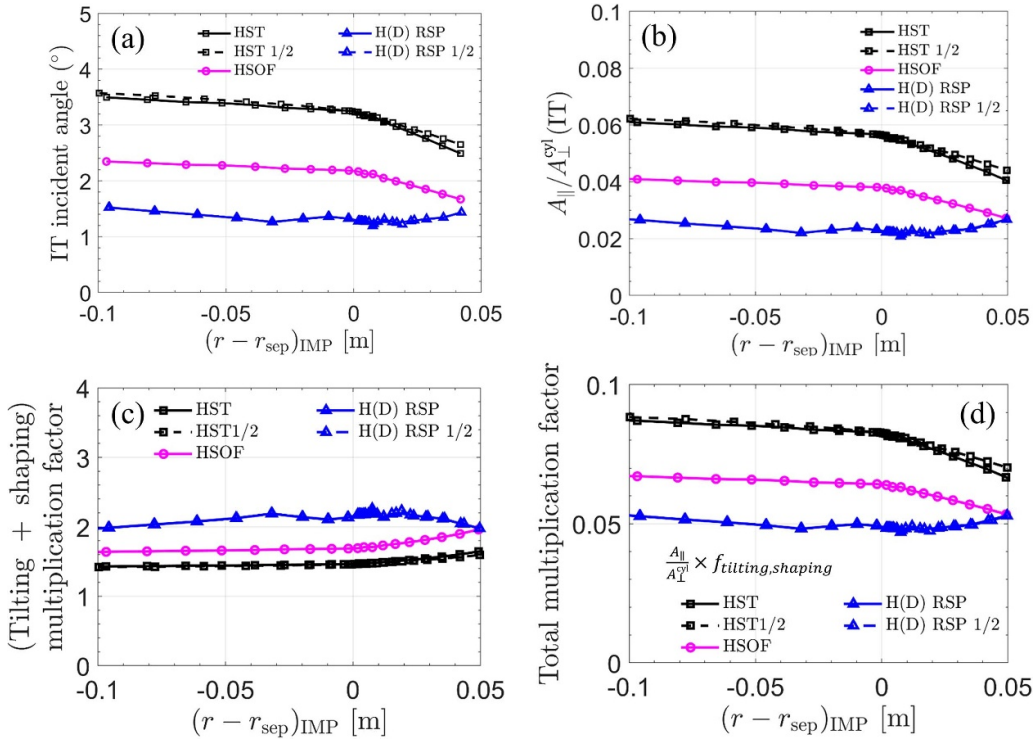

Figure 13. *(a)* Magnetic field line incident angle to the target surface without considering tilting and shaping *(b)* $A_{\parallel}/A_{\perp}^{\mathrm{cyl}}$ *(c)* $f_{\mathrm{tilt,shape}}$ *(d)* f_{total} as a function of distance from inner strike point mapped to inner mid-plane.

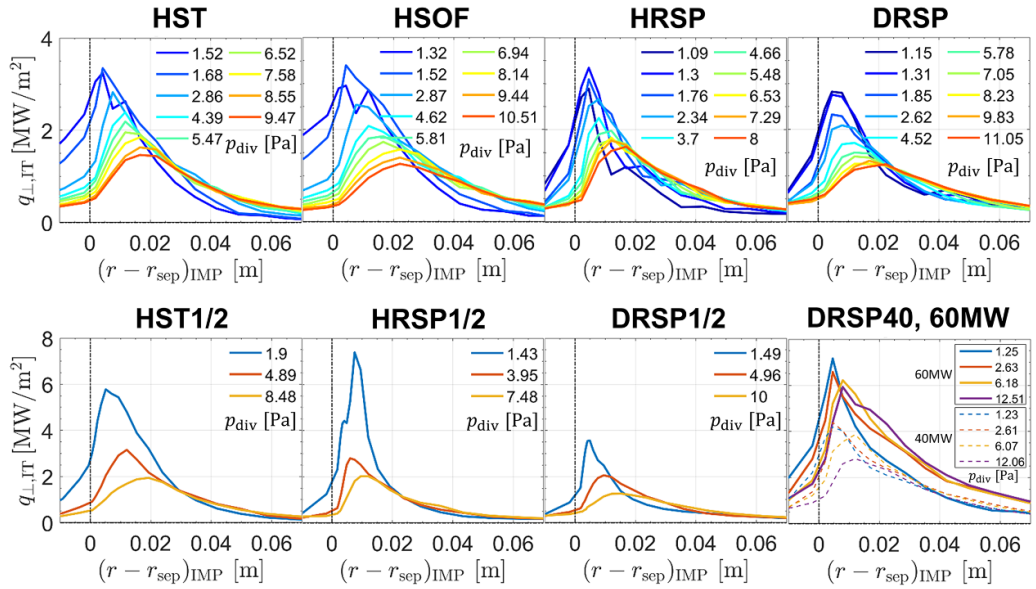

Figure 14. Target heat flux profile perpendicular to the target considering tilting and shaping as a function of distance from inner strike point mapped to inner mid-plane. The case name is shown above each subplots. The numbers in legend are p_{div}.

the neutral and radiation contributions are not affected by the anomalous perpendicular transport coefficients, the ratio and values of plasma, neutral, and radiation that contribute to $q_{\perp,\mathrm{IT}}$ are not significantly different from the standard transport cases. Therefore, in a raised strike point scenario aimed at removing tritium co-deposited on an inner vertical target, the impact of the uncertainty on the perpendicular transport (e.g. λ_q, as discussed in section 2) can be ignored when operating in a partially detached regime. The external heating power and fuel throughput are therefore the only relevant variables that can significantly affect the target heat flux.

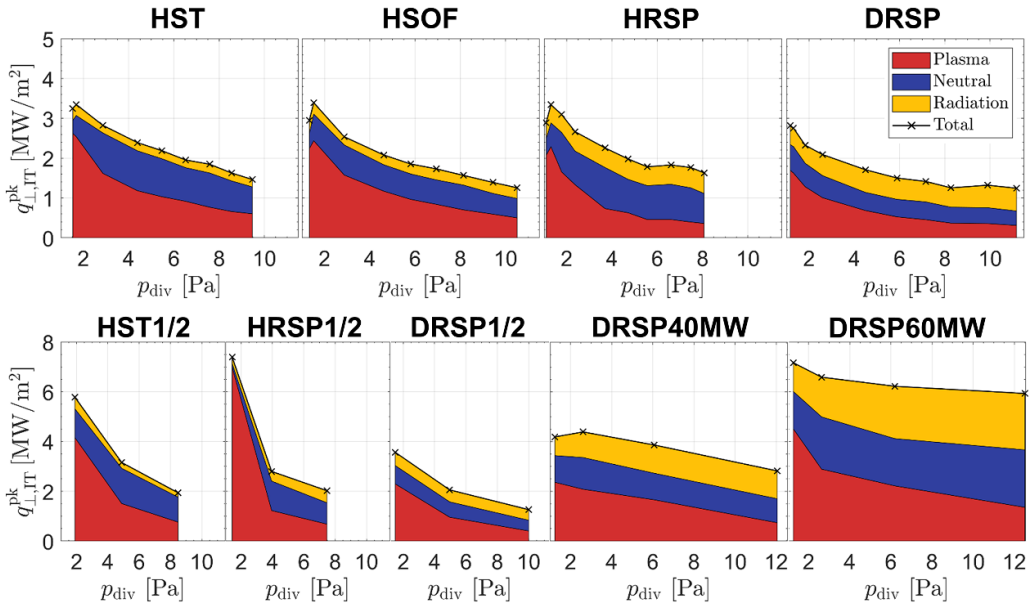

Figure 15. Peak perpendicular inner target heat flux decomposed into plasma, neutral and radiation contribution, as a function of p_{div}. The case series name is shown above each subplot.

4.2. Bulk tungsten monoblock surface temperature from FEM analysis

Based on the target heat flux provided by SOLPS-ITER, the temperature of the bulk tungsten monoblock surface was calculated using a simplified heat transfer model [35]. This model considers the 3D geometry of the ITER vertical divertor target monoblock including the CuCrZr tube in which the coolant flows, as well as the copper interlayer and tungsten body. The effect of the presence of the Be deposited layer is not considered at this stage, but will be addressed later. The shaping is applied on the top surface (1.0°) and the tilting is applied on the whole target (0.5°). The heat transfer calculation is split into 2D conduction within each monoblock (toroidal and radial directions) and the poloidal advection of the coolant by neglecting the poloidal conduction. The ITER coolant parameters are specified as a mass flow rate of 0.734 kg s^{-1} and a temperature of 70 °C [36]. For the detailed setup and boundary conditions of the heat transfer model, see section 3 in [35]. The IT surface temperature $T_{\mathrm{surf,IT}}$ is shown as a function of poloidal distance along the target from the corner with the inner reflector plate (bottom of the inner vertical wall) $L_{\mathrm{VT,pol}}$ (figure 16). For the cases with p_{div} =7–8 Pa, all cases except for the high powers (DRSP40MW, DRSP60MW) have a peak $T_{\mathrm{surf,IT}}$ lower than 200 °C. In the DRSP40MW and DRSP60MW cases, $T_{\mathrm{surf,IT}}$ is interpolated to be in a range of 200 °C–250 °C, and 350 °C–400 °C, respectively, when p_{div} =7–8 Pa.

A dedicated experiment [37] was performed, in which a Be–D co-deposited layer was exposed to D plasmas for 180 s (the time from SOR to EOD in the raised strike point scenario). The D removal fraction was about 30%, 50%, and 80%, respectively, for temperatures of 400 °C, 500 °C, and 600 °C. Therefore, if a surface temperature of at least 600 °C could be maintained for the full 180 s, it can be expected that up to 80% of the co-deposited tritium would be removed. If the surface temperature would be maintained at 500 °C, then a similar 80% tritium removal performance could be obtained if the exposure time were to be increased to about 1200 s. Such long exposure times may however be limited by the raised strike-point operational scenario constraints. Impurity-seeded discharges in raised strike point scenarios may enhance detritiation efficiency due to sputtering effects; however, in this paper, we have only considered deuterium-only or hydrogen-only scenarios.

However, according to the simulation results above, at 20 and 40 MW heating powers, the target surface temperature does not even reach the baking divertor surface temperature of 350 °C, i.e. the scenario provides no detritiation benefit. When the heating power is 60 MW, the maximum achievable surface temperature can be raised to as high as 400 °C, but even this does not meet the conditions for efficient tritium removal. Changes in active cooling conditions such as a drop of the mass flow rate or increasing the coolant temperature could increase the surface temperature without affecting the plasma parameters significantly (they would only affect thermally reflected molecular temperature). However, changing the active cooling condition from the baseline parameter would only be possible after a very systematic engineering evaluation to assess any additional risks this would incur.

4.3. Be co-deposit layer temperature considering poor thermal contact

The result of the previous section considered heating of the W monoblock surface, without taking into account the thermal properties of the co-deposited layers. The previous FEM calculation can be modified by including conduction and radiation from the layers. First, the layer temperature is

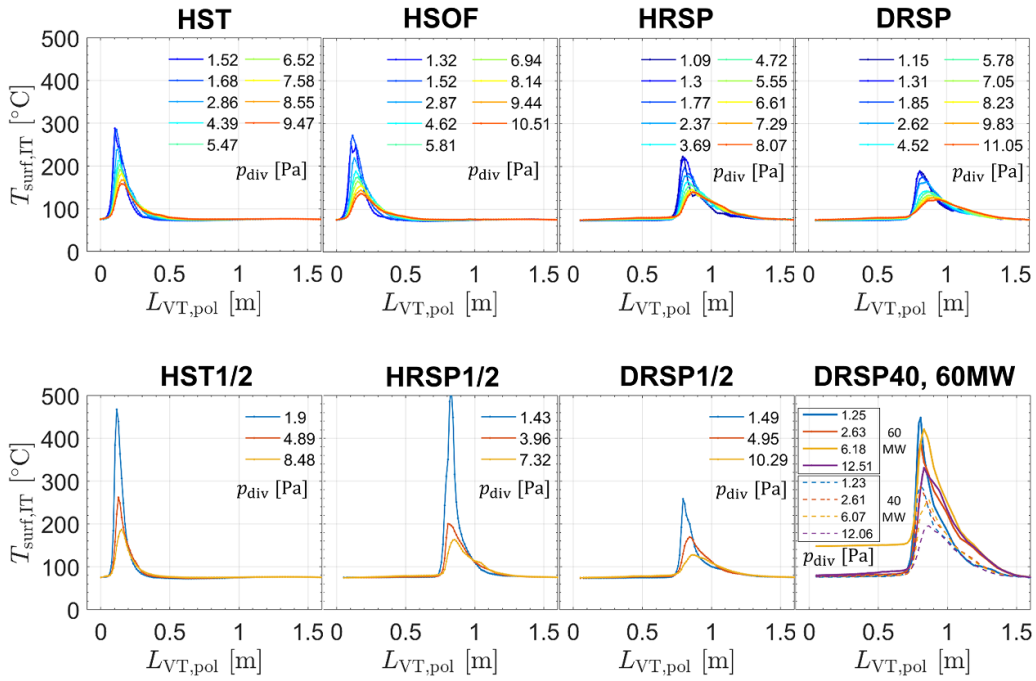

Figure 16. Inner target surface temperature profile is shown poloidally along the vertical target from the bottom. The case name is shown above each subplot. The numbers in the legend give the divertor neutral pressure p_{div}.

calculated in the no-radiation limit by considering conduction only. Hereafter, a temperature reduction by radiative cooling is discussed.

One can consider conduction through the Be co-deposit layer with some thermal contact resistance R_{th} between the layer and the tungsten monoblock surface:

$$R_{\mathrm{th}} = d/\lambda_{\mathrm{deposit}} + R_{\mathrm{c}} \tag{4}$$

where d is the thickness of the deposited layer, and $\lambda_{\mathrm{deposit}}$ is its thermal conductivity ($\sim$216 $\mathrm{Wm^{-1}\,K^{-1}}$ for beryllium bulk), and R_{c} is the thermal contact resistivity [38].

Considering a thick layer (100 μm), the conduction term comes to 5×10^{-7} $\mathrm{m^2\,KW^{-1}}$, which on its own raises the layer temperature by a few K considering the ITER target heat flux conditions. By introducing the contact resistance, the layer temperature result changes significantly. By using the incoming peak heat flux from the SOLPS-ITER simulations in the no-radiation limit (figure 15), considering the R_{c} and neglecting other processes, the upper limit of the T_{Be} at the $q^{\mathrm{pk}}_{\perp,\mathrm{IT}}$ location, $T^{\mathrm{pk,no-rad}}_{\mathrm{Be}}$, is given as follows:

$$T^{\mathrm{pk,no-rad}}_{\mathrm{Be}} = \begin{cases} 150 + R_{\mathrm{c}}\times(1.5\,\mathrm{MW})\ ^{\circ}\mathrm{C} & \text{for DRSP20MW} \\ 250 + R_{\mathrm{c}}\times(4.0\,\mathrm{MW})\ ^{\circ}\mathrm{C} & \text{for DRSP40MW} \\ 400 + R_{\mathrm{c}}\times(6.0\,\mathrm{MW})\ ^{\circ}\mathrm{C} & \text{for DRSP60MW} \end{cases}. \tag{5}$$

The minimum value of R_{c} required to reach a $T^{\mathrm{pk,no-rad}}_{\mathrm{Be}}$ of 600 °C sufficient for effective outgassing are 3×10^{-4} $\mathrm{m^2\,KW^{-1}}$, 8.75×10^{-5} $\mathrm{m^2\,KW^{-1}}$, 3.33×10^{-5} $\mathrm{m^2\,KW^{-1}}$ for DRSP20MW, DRSP40MW, DRSP60MW, respectively.

In JET-ILW experiments (JPN#98297), $R_{\mathrm{c}} = 5\times10^{-4}$ $\mathrm{m^2\,KW^{-1}}$ ($\pm$20%) was estimated from infrared measurements of the surface temperature, combined with thermocouple readings for the bulk material. The $q^{\mathrm{pk}}_{\perp}$ at the considered location was 1.9 $\mathrm{MW\,m^{-2}}$, which is similar to the DRSP20MW condition, leading to a surface temperature of 800 °C–1000 °C [12].

The R_{c} estimated from the JET experimental measurement satisfies the condition of achieving a peak layer temperature of 600 °C or more in all DRSP scenarios, and ignoring other processes, the following peak layer temperature in the no-radiation limit is obtained.

$$T^{\mathrm{pk,no-rad}}_{\mathrm{Be}} = \begin{cases} 750-1050\ ^{\circ}\mathrm{C} & \text{for DRSP20MW} \\ 1400-2000\ ^{\circ}\mathrm{C} & \text{for DRSP40MW} \\ 2730-3930\ ^{\circ}\mathrm{C} & \text{for DRSP60MW} \end{cases}. \tag{6}$$

These temperatures, even at the lowest heating power of 20 MW are sufficient to deplete the layers from tritium. At higher heating power, for the JET-like contact resistance, the surface temperature may rise even above the boiling point of Beryllium (2469 °C, measured at atmospheric pressure), which could pose potential risks for ITER.

The degree of radiative cooling of the Be layer can be inferred from the sum of the radiation from the Be layer into the vessel $q^{\mathrm{rad}}_{\mathrm{Be-vessel}}$ and the radiative heat transfer term $q^{\mathrm{rad}}_{\mathrm{Be-W}}$ between the Be layer and the bulk tungsten, assuming no other thermal contact:

$$\begin{aligned} q^{\mathrm{rad}}_{\mathrm{Be}} &= q^{\mathrm{rad}}_{\mathrm{Be-vessel}} + q^{\mathrm{rad}}_{\mathrm{Be-W}} \\ &= \sigma\epsilon_{\mathrm{Be}}T^4_{\mathrm{Be}} + \frac{\sigma(T^4_{\mathrm{Be}} - T^4_{\mathrm{W}})}{\frac{1}{\epsilon_{\mathrm{Be}}} + \frac{1}{\epsilon_{\mathrm{W}}} - 1}. \end{aligned} \tag{7}$$

Table 2. Radiative heat transfer between bulk tungsten surface and Be co-deposit layer. The third column assumes black body (BB) emissivity. Peak inner target heat fluxes at the $p_{\mathrm{div}} \sim 7$ Pa condition, and ratios with $q_{\mathrm{Be}}^{\mathrm{rad}}$ are shown.

Case name	$q_{\mathrm{Be}}^{\mathrm{rad}}$ (bulk max) $(\mathrm{MW m^{-2}})$	$q_{\mathrm{Be}}^{\mathrm{rad}}$ (BB limit) $(\mathrm{MW\,m^{-2}})$	$q_{\perp,\mathrm{IT}}^{\mathrm{pk}}(\mathrm{MW\,m^{-2}})$	$\frac{q_{\mathrm{Be}}^{\mathrm{rad}}}{q_{\perp,\mathrm{IT}}^{\mathrm{pk}}}$ (bulk max)	$\frac{q_{\mathrm{Be}}^{\mathrm{rad}}}{q_{\perp,\mathrm{IT}}^{\mathrm{pk}}}$ (BB limit)
DRSP20MW ($T_{\mathrm{Be}} = 880\,^{\circ}\mathrm{C}$, $T_{\mathrm{W}} = 150\,^{\circ}\mathrm{C}$)	4.32×10^{-2}	1.99×10^{-1}	1.5	2.9%	13%
DRSP40MW ($T_{\mathrm{Be}} = 1700\,^{\circ}\mathrm{C}$, $T_{\mathrm{W}} = 250\,^{\circ}\mathrm{C}$)	3.71×10^{-1}	1.71	4.0	9.3%	43%
DRSP60MW ($T_{\mathrm{Be}} = 3330\,^{\circ}\mathrm{C}$, $T_{\mathrm{W}} = 400\,^{\circ}\mathrm{C}$)	4.13	19.1	6.0	69%	330%

where $\sigma = 5.67 \times 10^{-8}\ \mathrm{Wm^{-2}K^{-4}}$ is the Stefan–Boltzmann constant, T the absolute temperature, and ϵ the emissivity. The radiation contribution from the vessel to the layer is neglected. The emissivities of Be and tungsten depend on the temperature and whether it is bulk material or a deposited layer. In case of a deposited layer, the emissivity also depends on the material of the deposition surface and the thickness of the layer. Here, among the values available in bulk W and Be, the maximum values $\epsilon_{\mathrm{Be}} = 0.33$ and $\epsilon_{\mathrm{W}} = 0.13$ are used [39]. The FEM results from the partially detached case were used, i.e. $T_{\mathrm{W}} = 150\,^{\circ}\mathrm{C}$, $250\,^{\circ}\mathrm{C}$, $400\,^{\circ}\mathrm{C}$ for the DRSP20MW, DRSP40MW, and DRSP60MW cases, respectively.

The no-radiation limit beryllium temperature in equation (6) is used to calculate an upper value for the radiative heat transfer in the maximum available bulk emissivity condition ($\epsilon_{\mathrm{Be}} = 0.33, \epsilon_{\mathrm{W}} = 0.13$). Also, the extreme upper bound of the $q_{\mathrm{Be-W}}^{\mathrm{rad}}$ is calculated in the blackbody limit ($\epsilon_{\mathrm{Be}} = \epsilon_{\mathrm{W}} = 1$) considering uncertainties in emissivity. The results are summarized in table 2. When the upper limit of $q_{\mathrm{Be}}^{\mathrm{rad}}$ is high compared to the heat flux from the plasma, it shows that the actual T_{Be} and T_{W} must be lower due to radiative cooling, and the final T_{Be} can be inferred through iteration.

The effect of radiation on T_{Be} can be identified by the ratio of $q_{\mathrm{Be}}^{\mathrm{rad}}$ and $q_{\perp,\mathrm{IT}}^{\mathrm{pk}}$. Assuming bulk maximum emissivity, $q_{\mathrm{Be}}^{\mathrm{rad}}$ is non-negligible only in the case of DRSP60MW so there will be some reduction of T_{Be} from the no-radiation limit of $T_{\mathrm{Be}} = 3330\,^{\circ}\mathrm{C}$. In the blackbody limit, a significant reduction of the T_{Be} is expected for the DRSP40MW and the DRSP60MW case while the effect of the radiation is still marginal for the case of DRSP20MW. If T_{Be} is 600 °C, $q_{\mathrm{Be}}^{\mathrm{rad}}$ is less than 1% and 5% of $q_{\perp,\mathrm{IT}}^{\mathrm{pk}}$ in bulk emissivity and BB limit, respectively. Therefore, a temperature of 600 °C for effective detritiation is achieved in all scenarios, even in the blackbody limit.

5. Conclusions

In this paper, SOLPS-ITER simulations were performed to evaluate a raised strike point scenario developed for the purpose of removing tritium co-deposited with Be on the upper part of the inner divertor target. Since the raised strike point scenario may differ from the standard PFPO-1 scenario in terms of plasma species, magnetic geometry, plasma current, heating power, anomalous transport coefficients (L-, H-mode), etc a divertor performance analysis was conducted for each case. As a result of these parameter scans, the following physical insights were obtained:

(i) HST vs. HSOF (parallel connection length effect)—By scaling the plasma current by 2/3, the connection length increases by factor of 1.5. The longer connection length means an increase of the parallel transport time scale. Hence, the effect of the perpendicular transport is expected to be larger. However, the target heat flux profile was not significantly different. Radial transport in the divertor is only significant in the 1st SOL flux tube next to the separatrix, in attached conditions [25]. Also, in the region below the X-point, broadening of the heat flux profile is less effective because of the higher flux expansion [40].

(ii) HST (or HSOF) vs. HRSP (neutral baffling effect: magnetic geometry, dome, corner shaped divertor)—By raising the strike point, the SOL and dome do not efficiently screen the recycled neutrals away from the X-point, unlike the ITER baseline magnetic configuration. Thus, in the RSP cases, the recycled neutrals can reach the entire PFR and provide an ionization source along the entire SOL-PFR boundary, whereas in the HST case the ionization is localized near the target due to the corner effect. Therefore, the divertor detaches for HRSP cases at lower p_{div} than for HST cases. Moreover, HRSP cases emit more radiation than the HST ones from an expanded radiation zone extending from the target to the X-point. The radiation heat load on the target compensates the contribution from the plasma so that the peak IT heat loads are similar although core-edge compatibility deteriorates when raising the strike point.

(iii) HRSP vs. DRSP (isotope effect from mass difference)—Since the thermal velocity of D is smaller than that of H, assuming the same first wall surface temperature, DRSP cases require a higher p_{div} than HRSP cases to achieve global particle balance for a given fuel throughput. In addition, D stays longer near the SOL-PFR boundary and the strike point where ionization occurs most actively, and therefore has a higher density over a larger area.

(iv) Standard transport vs. ½ transport—The anomalous transport coefficients affect the upstream density and peak target heat flux in attached conditions. However, as the plasma detaches, the divertor conditions are dominated

by the plasma–neutral interactions rather than the perpendicular transport so the peak target fluxes are not affected much by the choice of transport coefficient.

(v) DRSP (20MW) vs. DRSP40MW vs. DRSP60MW (auxiliary heating power)—The heating power governs many SOL and divertor parameters, such as density, ionization sources, and radiative cooling efficiency. It is the main determinant of the peak target heat flux, so it can be used as an actuator to change the target surface temperature.

Using the target heat fluxes computed by SOLPS-ITER, a simplified heat transfer analysis shows that the bulk tungsten target monoblock surface temperature can be raised up to 400 °C under partially detached conditions which remain safe from the point of view of tungsten sputtering. This is an insufficient temperature for efficient tritium outgassing. However, if one assumes that the Be co-deposit layer and the tungsten surface are in poor thermal contact with each other, the temperature of the layer can be significantly increased. The minimum requirement for thermal contact resistance to achieve Be co-deposit layer temperature greater than 600 °C with efficient tritium outgassing is in the range of about $3.33 \times 10^{-5} - 3 \times 10^{-4}$ depending on the scenario.

The thermal contact resistance estimated from the JET-ILW experimental measurements satisfies this condition, so even in the DRSP20MW scenario with the lowest bulk tungsten temperature and the peak heat flux, the temperature of the Be co-deposit can reach 750 °C–1050 °C, which would enable very efficient detritiation. Under such conditions, the raised strike point scenario could be used as an alternative detritiation method in the case of thick deposits at the inner divertor, as supported by the JET results [12]. While the thermal contact resistance estimated from JET-ILW experimental measurements satisfies this condition, it is worth noting that the required contact resistance might not be achieved under all scenarios and conditions, including those specific to ITER. Considering the thermal contact resistivity conditions obtained from JET-ILW experiments, even in the DRSP20MW scenario with the lowest bulk tungsten temperature and the peak heat flux, the temperature of the Be co-deposit can reach 750 °C–1050 °C, which would enable very efficient detritiation. Under conditions where the required contact resistance is achieved, the raised strike point scenario could be used as an alternative detritiation method for thick deposits at the inner divertor, as supported by the JET results [12].

Acknowledgments

This manuscript has been authored by UT-Battelle, LLC, with the US Department of Energy (DOE). Work supported in part by the US DOE under Contracts DE-AC05-00OR22725. This work was supported in part by the National R&D Program through the National Research Foundation of Korea (NRF), funded by the Ministry of Science and ICT (NRF-2019M1A7A1A03087560). The first author, J.-S. Park, is also supported through the Monaco/ITER postdoctoral fellowship program (2019–2020). The views and opinions expressed herein do not necessarily reflect those of the ITER Organization. The authors are grateful to Greg De Temmerman for the great help in initiating this study.

ORCID iDs

Jae-Sun Park https://orcid.org/0000-0003-0871-7527
Richard Pitts https://orcid.org/0000-0001-9455-2698
Tom Wauters https://orcid.org/0000-0002-2941-7817

References

[1] ITER Organization 2018 ITER research plan within the staged approach (level III—provisional version) *ITER Technical Report* (ITR-18-003) (available at: www.iter.org/technical-reports)
[2] De Temmerman G., Baldwin M., Anthoine D., Heinola K., Jan A., Jepu I., Likonen J., Lungu C., Porosnicu C. and Pitts R. 2017 Efficiency of thermal outgassing for tritium retention measurement and removal in ITER *Nucl. Mater. Energy* **12** 267–72
[3] Wauters T. *et al* 2020 Wall conditioning in fusion devices with superconducting coils *Plasma Phys. Control. Fusion* **62** 034002
[4] Roth J. *et al* 2008 Tritium inventory in ITER plasma-facing materials and tritium removal procedures *Plasma Phys. Control. Fusion* **50** 103001
[5] Romazanov J. *et al* 2020 First Monte–Carlo modelling of global beryllium migration in ITER using ERO2. 0 *Contrib. Plasma Phys.* **60** e201900149
[6] Schmid K., Krieger K., Lisgo S., Meisl G. and Brezinsek S. (JET Contributors) 2015 Walldyn simulations of global impurity migration in jet and extrapolations to ITER *Nucl. Fusion* **55** 053015
[7] Khan A., De Temmerman G., Lisgo S., Bonnin X., Anand H., Miller M., Pitts R., Schmid K. and Kukushkin A. 2019 Walldyn simulations of material migration and fuel retention in ITER low power H plasmas and high power neon-seeded DT plasmas *Nucl. Mater. Energy* **20** 100674
[8] Kolesnikov R., Bulmer R., LoDestro L., Casper T. and Pitts R. 2013 Equilibrium and vertical-instability considerations for vertical strike-point shifts on the ITER divertor targets *Nucl. Fusion* **53** 083021
[9] Khayrutdinov R. and Lukash V. 1993 Studies of plasma equilibrium and transport in a tokamak fusion device with the inverse-variable technique *J. Comput. Phys.* **109** 193–201
[10] Wiesen S. *et al* 2015 The new SOLPS-ITER code package *J. Nucl. Mater.* **463** 480–4
[11] Bonnin X., Dekeyser W., Pitts R., Coster D., Voskoboynikov S. and Wiesen S. 2016 Presentation of the new SOLPS-ITER code package for tokamak plasma edge modelling *Plasma Fusion Res.* **11** 1403102
[12] Wauters T. *et al* (JET Contributors) 2022 Isotope removal experiment in JET-ILW in view of T-removal after the 2nd DT campaign at JET *Phys. Scr.* **97** 044001
[13] Imbeaux F. *et al* 2015 Design and first applications of the ITER integrated modelling & analysis suite *Nucl. Fusion* **55** 123006
[14] Park J.-S., Bonnin X. and Pitts R. 2020 Assessment of ITER divertor performance during early operation phases *Nucl. Fusion* **61** 016021
[15] Veselova I., Kaveeva E., Rozhansky V., Senichenkov I., Poletaeva A., Pitts R.A. and Bonnin X. 2021 Solps-ITER drift modelling of ITER burning plasmas with narrow near-sol heat flux channels *Nucl. Mater. Energy* **26** 100870

[16] Scarabosio A., Eich T., Herrmann A. and Sieglin B. (The ASDEX Upgrade Team and JET-EFDA contributors) 2013 Outer target heat fluxes and power decay length scaling in L-mode plasmas at JET and AUG *J. Nucl. Mater.* **438** S426–30
[17] Chang C., Ku S., Hager R., Churchill R., Hughes J., Köchl F., Loarte A., Parail V. and Pitts R. 2021 Constructing a new predictive scaling formula for ITER's divertor heat-load width informed by a simulation-anchored machine learning *Phys. Plasmas* **28** 022501
[18] Eich T. *et al* 2013 Scaling of the tokamak near the scrape-off layer H-mode power width and implications for ITER *Nucl. Fusion* **53** 093031
[19] Pitts R. *et al* 2019 Physics basis for the first ITER tungsten divertor *Nucl. Mater. Energy* **20** 100696
[20] Uljanovs J. *et al* 2017 The isotope effect on divertor conditions and neutral pumping in horizontal divertor configurations in JET-ILW ohmic plasmas *Nucl. Mater. Energy* **12** 791–7
[21] Day C., Varoutis S. and Igitkhanov Y. 2016 Effect of the dome on the collisional neutral gas flow in the demo divertor *IEEE Trans. Plasma Sci.* **44** 1636–41
[22] Ziegler J.F., Ziegler M.D. and Biersack J.P. 2010 SRIM–the stopping and range of ions in matter (2010) *Nucl. Instrum. Methods Phys. Res.* B **268** 1818–23
[23] Krasheninnikov S. and Kukushkin A. 2017 Physics of ultimate detachment of a tokamak divertor plasma *J. Plasma Phys.* **83** 155830501
[24] Stangeby P. and Sang C. 2017 Strong correlation between D2 density and electron temperature at the target of divertors found in SOLPS analysis *Nucl. Fusion* **57** 056007
[25] Park J.S., Groth M., Pitts R., Bak J.-G., Thatipamula S., Juhn J.-W., Hong S.-H. and Choe W. 2018 Atomic processes leading to asymmetric divertor detachment in KSTAR L-mode plasmas *Nucl. Fusion* **58** 126033
[26] Kotov V. and Reiter D. 2009 Two-point analysis of the numerical modelling of detached divertor plasmas *Plasma Phys. Control. Fusion* **51** 115002
[27] Stangeby P. 2018 Basic physical processes and reduced models for plasma detachment *Plasma Phys. Control. Fusion* **60** 044022
[28] Pütterich T., Neu R., Dux R., Whiteford A., O'Mullane M. and Summers H. *et al* 2010 Calculation and experimental test of the cooling factor of tungsten *Nucl. Fusion* **50** 025012
[29] Eckstein W., Dohmen R., Mutzke A. and Schneider R. 2007 *SDTrimSP: Ein Monte-Carlo Code zur Berechnung von Stossereignissen in ungeordneten Targets* 12/3 Garching: Max-Planck-Institut für Plasmaphysik
[30] Kirschner A. *et al* 2019 Modelling of tungsten erosion and deposition in the divertor of JET-ILW in comparison to experimental findings *Nucl. Mater. Energy* **18** 239–44
[31] Huber A. *et al* 2021 Understanding tungsten erosion during inter/intra-ELM periods in He-dominated JET-ILW plasmas *Phys. Scr.* **96** 124046
[32] Tskhakaya D. and Groth M. *et al* 2015 Modelling of tungsten re-deposition coefficient *J. Nucl. Mater.* **463** 624–8
[33] Kirschner A., Tskhakaya D., Brezinsek S., Borodin D., Romazanov J., Ding R., Eksaeva A. and Linsmeier C. 2017 Modelling of plasma-wall interaction and impurity transport in fusion devices and prompt deposition of tungsten as application *Plasma Phys. Control. Fusion* **60** 014041
[34] Mellet N., Gunn J., Pégourié B., Marandet Y., Martin C. and Roubin P. 2017 Tungsten erosion by impurities and redeposition: focus on the magnetised sheath *Plasma Phys. Control. Fusion* **59** 035006
[35] Carli S., Pitts R.A., Bonnin X., Subba F. and Zanino R. 2018 Effect of strike point displacements on the ITER tungsten divertor heat loads *Nucl. Fusion* **58** 126022
[36] Seki Y., Ezato K., Suzuki S., Yokoyama K., Yamada H., Hirayama T. and Hirai T. 2018 Numerical and experimental study of coolant water flow in ITER divertor outer vertical target *Fusion Eng. Des.* **136** 420–5
[37] Založnik A., Doerner R.P. and De Temmerman G. 2020 Deuterium removal from beryllium co-deposits by simulated strike-point sweeping *Nucl. Mater. Energy* **24** 100750
[38] Gaspar J., Rigollet F., Gardarein J.-L., Le Niliot C. and Corre Y. 2016 *In-situ* estimation of the thermal resistance of carbon deposits in the JET tokamak *Int. J. Therm. Sci.* **104** 292–303
[39] Ruset C., Falie D., Grigore E., Gherendi M., Zoita V., Zastrow K.-D., Matthews G., Courtois X., Bucalossi J. and Likonen J. *et al* 2017 The emissivity of W coatings deposited on carbon materials for fusion applications *Fusion Eng. Des.* **114** 192–5
[40] Gallo A., Fedorczak N., Maurizio R., Theiler C., Elmore S., Labit B., Reimerdes H., Nespoli F., Ghendrih P. and Eich T. *et al* 2017 Effect of plasma geometry on divertor heat flux spreading: Monalisa simulations and experimental results from TCV *Nucl. Mater. Energy* **12** 893–8